

Developing Force Fields for Accurate Mg^{2+} and Triphosphate

Interactions in $\text{ATP}\cdot\text{Mg}^{2+}$ and $\text{GTP}\cdot\text{Mg}^{2+}$ Complexes

Fangchen Hu[†], Yuwei Zhang[‡], Pengfei Li[†], Ruibo Wu[⊥] and Fei Xia^{*†}

[†]*School of Chemistry and Molecular Engineering, NYU-ECNU Center for Computational Chemistry at NYU Shanghai, East China Normal University, Shanghai 200062, China*

[‡]*Jiangsu Key Laboratory of New Power Batteries, Jiangsu Collaborative Innovation Centre of Biomedical Functional Materials, School of Chemistry and Materials Science, Nanjing Normal University, Nanjing 210023, P. R. China.*

[†]*Department of Chemistry and Biochemistry, Loyola University Chicago, 1068 W. Sheridan Rd., Chicago, Illinois 60660, United States*

[⊥]*School of Pharmaceutical Sciences, Sun Yat-sen University, Guangzhou 510006, China*

Abstract

In cells, adenosine triphosphate (ATP) and guanosine triphosphate (GTP) molecules typically form tri-coordinated or bi-coordinated $\text{ATP}\cdot\text{Mg}^{2+}$ or $\text{GTP}\cdot\text{Mg}^{2+}$ complexes with Mg^{2+} ions and bind to proteins, participating in and regulating many important cellular functions. The accuracy of their force field parameters plays a crucial role in studying the function-related conformations of $\text{ATP}\cdot\text{Mg}^{2+}$ or $\text{GTP}\cdot\text{Mg}^{2+}$ using molecular dynamics (MD) simulations. The parameters developed based on the methyl triphosphate model in existing AMBER force fields cannot accurately describe the conformational distribution of tri-coordinated or bi-coordinated $\text{ATP}\cdot\text{Mg}^{2+}$ or $\text{GTP}\cdot\text{Mg}^{2+}$ complexes in solution. In this study, we develop force field parameters for the triphosphate group based on the new ribosyl triphosphate model, considering dihedral coupling effect, accurate van der Waals (vdW) interactions, and the influence of strongly polarized charges on conformational balance. The new force fields can accurately describe the conformational balance of tri-coordinated and bi-coordinated $\text{ATP}\cdot\text{Mg}^{2+}$ or $\text{GTP}\cdot\text{Mg}^{2+}$ conformations in solution and can be applied to simulate biological systems containing $\text{ATP}\cdot\text{Mg}^{2+}$ or $\text{GTP}\cdot\text{Mg}^{2+}$ complexes.

1. INTRODUCTION

Nucleotide polyphosphate molecules such as ATP (adenosine triphosphate) and GTP (guanosine triphosphate) are essential participants in numerous biochemical reactions within cells, playing crucial roles in various life processes.^{1,2} Both molecules share a common structural feature: a nucleoside linked to a triphosphate group, as illustrated in **Figure 1**. When they form complexes with proteins in cells, they typically coordinate with metal cations, such as Mg^{2+} or Ca^{2+} .^{3,4} The α -, β -, and γ -O atoms in the triphosphate moiety of ATP and GTP can adopt either a tridentate (C3) or bidentate (C2) coordination conformation with Mg^{2+} . Early nuclear magnetic resonance (NMR) and spectroscopic studies^{5, 6} on the conformations of $\text{ATP}\cdot\text{Mg}^{2+}$ and $\text{GTP}\cdot\text{Mg}^{2+}$ in solution revealed the existence of both C3 and C2 coordination forms. These two conformations can interconvert in solution. The conformation distribution measured in NMR experiments suggested a minimal free energy difference, $\Delta G_{\text{C23}} = \Delta G_{\text{C2}} - \Delta G_{\text{C3}}$ between the C2 and C3 conformations.

To support simulation studies on the biological functions of ATP and GTP molecules, several research groups have made significant contributions to developing force fields for polyphosphate molecules.⁷⁻¹¹ Weiner et al.⁷ and Pavelites et al.⁹ systematically developed the force fields for polyphosphates, facilitating the simulation of complex systems such as nucleotides. Meagher et al.¹² advanced these efforts by developing polyphosphate force fields specifically for simulating ATP molecules, using the methyl triphosphate (MTP) model and fitting potential energy surfaces of dihedral angles derived from quantum mechanics (QM) calculations. Buelens et al.¹³ applied ATP force field parameters to simulate the conformational transition between the C3 and C2 states of $\text{ATP}\cdot\text{Mg}^{2+}$ complexes. However, comparisons of the potential of mean force (PMF) profiles of $\text{ATP}\cdot\text{Mg}^{2+}$ obtained from the AMBER¹² and CHARMM22⁹ force fields revealed a significant discrepancy, with the predicted free energy difference between the C2 conformations exceeding 12.0 kcal/mol.¹³

The ΔG_{C23} for the $\text{ATP}\cdot\text{Mg}^{2+}$ complex obtained from AMBER force field simulations is approximately 7.8 kcal/mol (**Figure S1 of Supporting Information (SI)**), which underestimates the stability of the C2 conformation. The energy barrier

between the calculated C3 conformation and the transition state (TS) is as high as 17.0 kcal/mol. In contrast, the ΔG_{C23} result from CHARMM22 force field simulations by Branduardi et al.¹⁴ is around -5.0 kcal/mol, overestimating the stability of the C2 conformation, with the energy barrier between the C3 conformation and TS around 8.7 kcal/mol. Additionally, they reported a ΔG_{C23} value of approximately -2.4 kcal/mol using the CHARMM27 force fields, with an energy barrier between the C3 and TS structures of about 13.8 kcal/mol. Moreover, Komuro et al.¹⁵ refined the parameters of the P-OS-P angles in phosphate groups within the CHARMM27 force field using high-level MP2 calculations, resulting in corrected parameters that accurately described the P-OS-P bond angle distribution of ATP molecules in crystal structures.

As mentioned earlier, the phosphate group in the current AMBER force field¹² struggles to accurately describe the distribution of the C3 and C2 conformations of ATP·Mg²⁺ complexes in solution. Several factors may contribute to these inaccuracies: First, the original force field parameters were derived from the MTP model,¹² which did not adequately capture the influence of the ribosyl ring on the phosphate group conformation. We propose developing a new model that includes the ribosyl ring. Second, the dihedral angle parameters for the phosphate group in the original force field were fitted only to one-dimensional (1D) potential energy curves, without accounting for dihedral coupling effects. Tian et al. successfully applied the grid-energy correction map (CMAP)^{16,17} to parametrize backbone dihedral angles in the AMBER19SB¹⁸ force fields, significantly improving the accuracy of dihedral descriptions. We plan to use CMAP to describe the dihedral interactions within the triphosphate group as well. Additionally, the non-bonded interaction parameters inherited from the earlier AMBER94/99^{8,19} force fields, which describe the interaction between Mg²⁺ ions and triphosphate oxygen atoms, may not accurately represent these interactions. Therefore, we will refine the vdW parameters for Mg²⁺ ions and phosphate oxygen atoms based on precise density functional theory (DFT) calculations.^{20,21} Considering these reasons, we aim to develop new parameters for the phosphate groups of ATP and GTP in the AMBER force field and explore the relevant energetic factors on conformational distribution.

2. Methods and Simulation Details

2.1 Potential Energy Surface Scans

The original MTP model¹² was extended to include a ribosyl ring, capped it with a hydrogen atom, resulting in the ribosyl triphosphate (RTP) model, as shown in **Figure 1**. We employed the HF/6-31+G* and MP2/6-31+G* methods in the Gaussian16²² QM package to recalculate potential energy curves of the six dihedral angles in the MTP model, as listed in **Table 1**. The potential energy surfaces (PES) were calculated based on the optimized MTP structures by rotating the dihedral angles in 10-degree increments. The PES scans with the HF and MP2 methods resulted in 37 data points for the MTP model (**Figure S2 of SI**). For the RTP model, the original OS atom type of the O5' atom was designated with a new OY type, resulting in eight specific types of the dihedral angles. We used the same HF/6-31+G* level to perform PES scans at 15-degree intervals for the six dihedral angles of the RTP model and obtained the PES curves in **Figure 2**.

The calculated QM energy E_l^{QM} for the l^{th} dihedral angle in the RTP model was fitted to the corresponding molecular mechanics (MM) energy E_l^{MM} using the Amber built-in program *paramfit*²³ according to eq.(1):

$$\chi_1^2 = \sum_{l=1}^N \omega_l \left[(E_l^{QM} - E_l^{MM})^2 + K \right] \quad (1)$$

In eq.(1), the residual χ_1^2 is defined to minimize the squared difference of the E_l^{MM} and E_l^{QM} energies. The constant K compensates for the variations between the QM and MM energies, and the parameter ω_l is a scaling factor set to 1.0. The energy terms in E_l^{MM} are presented in eq.(2):

$$E_l^{MM} = \sum_{\text{Bonds}} K_b (b - b_0)^2 + \sum_{\text{Angles}} K_b (b - b_0)^2 + \sum_{\text{Dihedrals}} \frac{V_n}{2} (1 + \cos(n\theta - \delta)) \\ + \sum_{\text{Nonbonded}} \left(\frac{A_{ij}}{r_{ij}^{12}} - \frac{B_{ij}}{r_{ij}^6} + \frac{q_i q_j}{r_{ij}} \right) \quad (2)$$

The first and second terms represent harmonic bond and angle interactions, where K_b and K_θ are the force constants, and b_0 and θ_0 are the equilibrium values of bonds and angles, respectively. The cosine functions in the third term describe dihedral angle

interactions, with the parameters V_n , n , and δ representing the energy barriers, the periodicity, and the phase of dihedral angles, respectively.

A two-dimensional (2D) CMAP (2D-CMAP)^{16, 17} was calculated using the HF/6-31+G* method by scanning two adjacent dihedrals at 15-degree intervals, resulting in a total of 576 data points. In AMBER, the CMAP grid is represented using a bicubic spline function, as shown in eq.(3):

$$U_{cmap}(\varphi, \psi) = \sum_{i=0}^3 \sum_{j=0}^3 a_{ij} \varphi^i \psi^j \quad (3)$$

In eq.(3), a_{ij} are the coefficients, and both φ and ψ are dihedral angles measured in radians. More details about the 2D-CMAP can be found in previous references.¹⁸ It is supported in the pmemd.cuda in AMEBER18.²⁴ The fourth term consists of the vdW and electrostatic interactions. A_{ij} and B_{ij} are the parameters for the pairwise atoms i and j in a 12-6 Lennard-Jones (LJ) potential,²⁵ while q_i and q_j represent the atomic charges of atoms i and j for electrostatic interaction.

2.2 Deviation of Parameters and RESP Charges

To develop accurate LJ parameters A_{ij} and B_{ij} in eq.(2) for Mg^{2+} -O coordination interactions, we adopted an approach similar to that utilized in the development of the AMOEBA+ force field.²⁶ The method involves parameterizing nonbonded vdW interactions using the exchange-repulsion and dispersion-like energies calculated from high-level DFT methods. It is important to note that the dispersion interaction, as defined in the widely used energy decomposition analysis (EDA) based on the symmetry-adapted perturbation theory (SAPT) method,^{20, 21} includes the entire Coulomb correlation and dispersion correction energies.

We employed a distinct EDA scheme known as the sobEDA method²⁷ for energy decomposition. In the sobEDA method, the sum of the exchange energy ΔE_x and the repulsion energy ΔE_{rep} is defined as the exchange-repulsion interaction ΔE_{xrep} . The sum of the DFT correction energy E_{DFTc} and the dispersion correlation ΔE_{dc} is defined as the dispersion-like Coulomb correlation ΔE_c . Lu et al.²⁷ suggested that the combined energies of E_{xrep} and ΔE_c in the sobEDA method appropriately

correspond to the exchange-repulsion correlation and dispersion correction energies in the SAPT method when using the accurate B3LYP-D3BJ functional.²⁸⁻³⁰ Therefore, we used the summed energies of ΔE_{xrep} and ΔE_c to derive the vdW parameters between the Mg^{2+} ion and the other atoms in ATP.

To reduce computational cost, we initially utilized a simplified RTP· Mg^{2+} model instead of the entire ATP· Mg^{2+} complex to perform umbrella sampling (US)³¹ simulations for the conformational change from the C3 to C2 structures. A total of 216 conformations were then randomly extracted from the different windows of the US simulation, including C3, C2, and transition state (TS) structures. Next, 216 single-point energy calculations were conducted on these structures using the accurate B3LYP-D3BJ/6-31+G** method. The sobEDA method²⁷ was employed for energy decomposition to obtain the ΔE_{xrep} and ΔE_c energies from single-point calculations. Finally, a least-square fitting was performed using the gradient descent method to minimize the residual χ_2^2 defined in eq.(5):

$$\chi_2^2 = \sum_{m=1}^{M=216} \left(E_m^{QM,vdW} - \sum_{n=1}^{N=30} E_{m,n}^{MM,vdW} \right)^2 \quad (4)$$

In eq.(4), the first term $E_m^{QM,vdW}$ represents the QM energy sum of ΔE_{xrep} and ΔE_c calculated from the m^{th} structure among the $M = 216$ conformations using the B3LYP-D3BJ/6-31G+G* method. The second term $E_{m,n}^{MM,vdW}$ denotes the molecular mechanics (MM) vdW interaction energies between the Mg^{2+} ion and the other $N = 30$ atoms of the RTP model in the m^{th} structure. Minimizing χ_2^2 serves to optimize the vdW parameters A_{ij} and B_{ij} indicated in eq.(2) for Mg^{2+} and ATP.

For the electrostatic interactions, the original atomic charges of ATP used in the AMBER force fields are based on RESP¹⁹ charges calculated using the HF/6-31+G* method. As an alternative, we propose using the B3LYP-D3BJ/6-311+G** method combined the PCM model,³² using a dielectric constant 78.35, to calculate the RESP charges of ATP. The atomic charges are determined using the standard RESP procedure.

2.3 MD Simulation Details and Umbrella Sampling

The C3 conformation of the ATP·Mg²⁺ complex was extracted from the crystal structure 1B38³³ and served as the initial structure in our simulations. The ATP·Mg²⁺ complex was immersed in a TIP3P³⁴ water box with a length of 14 Å and neutralized with two Na⁺ ions. The ATP parameters developed by Meagher et al.¹² and the compromise Mg²⁺ parameters developed by Li et al.³⁵ were used for the ATP·Mg²⁺ complex. The SHAKE³⁶ algorithm was employed to maintain constraints on hydrogen-containing bonds. A non-bonded cutoff of 10 Å was applied, and long-range electrostatic interactions were treated using the Particle Mesh Ewald³⁷ method. The whole system underwent energy minimization, followed by heating in the NVT ensemble. The temperature was maintained at 300 K using a Langevin thermostat³⁸ with a collision frequency of 2.0 ps⁻¹, and the pressure was maintained at 1.0 bar using the Berendsen barostat.³⁹ The system was then equilibrated in the NPT ensemble at 300 K with an integration step of 2.0 fs, utilizing the Amber ff14SB⁴⁰ force fields within the AMBER18 package.²⁴

In the US simulation, the distance between the Mg²⁺ ion and the O_α atom, denoted as Mg²⁺-O_α, was selected as the 1D reaction coordinate. The Mg²⁺-O_α distance ranges from 1.7 to 5.9 Å, consistent with values used in previous simulations.¹³ This range was divided into 43 windows with a 0.1 Å interval. In each window, a 5 ns US simulation was conducted using a harmonic potential applied to the Mg²⁺-O_α distance, with a force constant of 150 kcal·mol⁻¹·Å⁻². The US trajectories were then used to generate 1D potential of mean force (PMF) curves using the WHAM method.⁴¹

2.4 Replica-Exchange MD (REMD) Simulations and Analysis

A total of 22 replicas spanning a temperature range of 300–420 K were employed for 150 ns REMD simulations.⁴² The temperatures for each replica were generated using a tool available at <https://jerkwin.github.io/gmxttools>. The REMD simulations were initiated from the C3 structures of the ATP·Mg²⁺ complex. We used the pypdb library to gather 1685 ATP·Mg²⁺ complexes in proteins from the PDB database, focusing on the C2 and C3 conformations. Principal component analysis (PCA) was performed on the backbones of triphosphate groups in ATP and the Mg²⁺ ions using the

CPPTRAJ⁴³ module in the AMBER18 package. The first two components, PC1 and PC2, were used as coordinates to construct two-dimensional free energy landscapes (2D-FELs). The crystal structures of 1685 ATP·Mg²⁺ complexes and the REMD trajectories were projected onto the 2D-FELs to yield the distributions of the C3 and C2 structures using the WHAM method.⁴¹

3. Results and Discussion

3.1 The Ribosyl Triphosphate (RTP) Model

We initially employed HF/6-31+G* to recalculate the 1D potential energy curves of the six dihedral angles previously calculated by Meagher et al.¹² The HF-calculated curves (**Figure S2 of SI**) align perfectly with their published results. To assess the impact of high-level methods on the calculation of dihedral angle potential energy curves, we applied the MP2/6-31+G* method for more accurate energy calculations, using the HF-optimized structures as a basis. The resulting black curves (**Figure S2 of SI**) exhibit no significant differences from those obtained with HF/6-31+G*. This suggests that simply employing a high-level method does not substantially improve the computational results. Consequently, we propose developing a new model to parameterize the triphosphate groups in ATP and GTP molecules.

As shown in **Figure 1**, the triphosphate groups in actual ATP or GTP molecules are connected to ribose rings. In the MTP model, a hydrogen atom was used to cap the C5' atom in place of the ribose, which failed to reflect the steric influence of ribose on the dihedral angles of the triphosphate group. In this work, we propose using the ribosyl triphosphate (RTP) model instead of the MTP model for parameterizing the triphosphate group. The advantage of the RTP model lies in its inclusion of the ribose moiety, allowing it to better capture the influence of ribose on the conformations of triphosphate group. Despite the increased number of atoms in the RTP model compared to the MTP model, and the minimal difference observed between the PES curves calculated by HF and MP2, we opted to use the HF/6-31+G* method for PES calculations on the crucial dihedral angles in the RTP model.

Figure 2 display the results of restrained PES scans for dihedral angles in the RTP model. In **Figure 2a** and **2b**, the curves for the dihedrals O1G-PG-O3B-PB and PG-O3B-PB-O3A show minimal differences compared to those from the MTP model. However, the energy curves for the dihedral angles O3B-PB-O3A-PA, PB-O3A-PA-O5', O3A-PA-O5'-C5', and PA-O5'-C5'-C4' in **Figures 2c-2f** exhibit notable differences, especially in **Figures 2e** and **2f**, where discrepancies with the MTP model are particularly pronounced. In **Figure 2e**, the MTP curve shows two minima at approximately 70 ° and 310 °, with identical energies. In contrast, the RTP model has two unequal minima, with the result at 310 ° being approximately 15.0 kcal/mol higher than that of the MTP model. In **Figure 2f**, the PA-O5'-C5'-C4' dihedral angle in the MTP model exhibits three energy minima due to the periodicity of the methyl group, located at 60 °, 180 °, and 300 °, respectively. By contrast, the RTP model presents two unequal minima at 90 ° and 225 °. This discrepancy is clearly attributed to the presence of the ribose moiety in the RTP model, which introduces a strong steric effect on the rotation of the PA-O5'-C5'-C4' dihedral angle, thereby eliminating the pseudo-periodicity of the methyl group observed in the MTP model.

3.2 Dihedral Parameters for the RTP Model

Based on the energy curves of the RTP model in **Figure 2**, we used the *paramfit* program to optimize the parameters for the P-OS-P angle and dihedral types according to eq.(1). The average RMSD value of the fitted data compared to the RTP model (**Figure S3** of **SI**) is 1.46 kcal/mol. **Table 1** lists the new parameters for the dihedrals and angle fitted to the PES curves of the RTP model. For comparison, the original parameters of the MTP model are also included in **Table 1**. The MTP model, shown in **Figure 1**, has six dihedral types, where the O5', O3A, and O3B atoms belong to the atom type OS. However, in the RTP model, the heterogeneous environment of the O5' atom differs from that of the O3A and O3B atoms. Therefore, we designated a new atom type OY for the O5' atom in the RTP model. Consequently, the P-OS-P-OS dihedral type in the MTP model split into two types of dihedrals: P-OS-P-OS and P-OS-P-OY. The specific dihedral PB-O3A-PA-O5' is now categorized under the new

dihedral type P-OS-P-OY. Additionally, the original dihedral types CT-OS-P-O2, CT-OS-P-OS, and HC-CT-OS-P were renamed as CT-OY-P-O2, CT-OY-P-OS, and HC-CT-OY-P, respectively. As a result, the RTP model includes a total of seven dihedral angles and an angle type P-OS-P.

Comparing the derived dihedral parameters of both models reveals significant difference due to substantial structural variations. The equilibrium value of the angle P-OS-P obtained from our fitting is 142.9° , which is close to the 150.0° value of the MTP model.¹² To validate these parameters, we conducted US simulations to estimate the PMF curve for the ATP·Mg²⁺ transition from the C3 to C2 conformations. In **Figure 3a**, the black curve was obtained using the original parameters of the MTP model,¹² while the red curve for the RTP model utilized the new parameters listed in **Table 1**. Both the MTP and RTP curves indicate that the Mg²⁺-O_α distance in the stable C3 conformation is approximately 1.9 Å. However, the most stable C2 conformation for the MTP model is located at an Mg²⁺-O_α distance of around 3.9 Å, whereas for the RTP model, it is around 4.8 Å.

We collected 1685 ATP·Mg²⁺ complexes from various crystal structures, which includes 519 C3 conformations and 1142 C2 conformations. **Figure 3b** shows the normalized histogram distributions of Mg²⁺-O_α distances for these complexes. The C3 conformations exhibit a sharp distribution, with 5.5% of them at approximately 2.0 Å, while the C2 conformations show a broader distribution of Mg²⁺-O_α distances ranging from 4.0 to 5.0 Å, with percentages beyond 6.0%. Both the MTP and RTP curves in **Figure 3a** appear relatively flat in the range of 4.0-5.0 Å, aligning reasonably well with the distributions presented in **Figure 3b**. Although the ribose ring was involved in the RTP model, the energies of the C3 conformations in this model were slightly lowered than those in the MTP model. Further improvements in the free energy change ΔG_{C23} are anticipated based on the RTP model.

3.3 The Grid-Energy Correction Map

To accurately account for the influence of dihedral angle changes on conformations, it is essential to consider coupled effects among dihedral interactions in

MD simulations. As shown in **Figures 2c-2f**, the 3th, 4th, 5th, and 6th dihedrals of the RTP model exhibit significant changes due to the presence of the ribose moiety. Therefore, we concentrated on the coupled interactions of the three pairs of the dihedrals: the 3th and 4th, 4th and 5th, 5th and 6th dihedrals. Using the HF/6-31+G* method, we conducted 2D PES scans for the three pairs of dihedrals, resulting in the reaction of three corresponding CMAPs: CMAP₃₄, CMAP₄₅, and CMAP₅₆. However, due to the convergence issues encountered in restricted calculations, we have only obtained a complete 2D CMAP₃₄ presented in **Figure 3c**. The other two CMAP₄₅ and CMAP₅₆ (**Figure S4** of **SI**) are incomplete. Since using incomplete 2D-CMAPs could result in arbitrary and potentially inaccurate outcomes, we decided to incorporate only the complete 2D CMAP₃₄ in the subsequent MD simulations.

The 2D CMAP₃₄ in **Figure 3c** provides valuable energetic insights into the interactions between the two adjacent dihedrals, O3B-PB-O3A-PA and PB-O3A-PA-O5'. Using this information, we re-estimated the PMF curve by including the CMAP₃₄ in US simulations. The resulting PMF curve, displayed as the blue curve shown in **Figure 3a**, shows significant differences compared to the red curve without incorporating the CMAP₃₄. Notably, the blue curve appears smoother and lower in energy in the Mg²⁺-O_α distance range of 4.0-5.0 Å. It reveals two relatively stable energy minima at distances of 4.0 and 5.5 Å. The free energy difference ΔG_{C23} measured from the blue curve is approximately 5.3 kcal/mol, which is 1.8 kcal/mol lower than the 7.1 kcal/mol observed in the red curve. These results indicate that incorporating dihedral interactions through the CMAP method effectively reduced the difference in conformational free energies between C2 and C3 conformations. However, the TS energy barrier has an unreasonable value of 16.2 kcal/mol. Further considerations of other factors influencing conformational equilibria may be necessary.

3.4 Refinement of Nonbonded Parameters from QM Calculations

In the previous simulation of ATP·Mg²⁺ complexes,¹³ the vdW parameters for Mg²⁺ ions and O atoms were derived from the optimized parameters for Mg²⁺ provided by Li et al.³⁵ and from the O, P atom parameters in the ABMER94/99 force fields. However,

the accuracy of these vdW parameters in describing the Mg^{2+} -O coordination interactions has not been verified. Inspired by the sobEDA method used by Liu et al.²⁶ for developing vdW parameters for the AMOEBA+ force field, we aim to parameterize vdW interactions using exchange-repulsion and dispersion energies obtained from accurate QM calculations.

To reduce computational cost, we initially utilized a simplified ATP· Mg^{2+} model, referred to as the RTP· Mg^{2+} model, for US simulations. We then randomly sampled 216 conformations from the trajectories across different US windows, including the C3, C2, and TS structures during conformational transition. Single-point energy calculations for these structures were performed using the accurate B3LYP-D3BJ/6-31+G* method. The sobEDA method²⁷ was employed to decompose the energy into exchange-repulsion energy ΔE_{xrep} and dispersion correction energy ΔE_{dc} , resulting in the summed QM energy $E^{QM,vdW}$. Finally, a least-square fitting was conducted on the $E^{QM,vdW}$ and $E^{MM,vdW}$ data, according to eq.(4). The derived pairwise parameters A_{ij} and B_{ij} for the 12-6 LJ potential interactions between Mg^{2+} ions and the O and P atom types are represented in **Table 2**. The results indicate that the A_{ij} values for the O3 and O2 types differ significantly between the original and QM-derived parameters, with the original A_{ij} being 26767.87 kcal·Å¹²/mol and the QM-derived being 56958.78 kcal·Å¹²/mol. However, the A_{ij} and B_{ij} parameters for the pairwise interactions involving Mg^{2+} ions with OS, OY, and P atoms show no significant difference.

Figure 4a compares the $E^{MM,vdW}$ data calculated using both the original and QM-derived LJ parameters. It is evident that the original LJ parameters significantly underestimated the total exchange-repulsion and dispersion interaction energies between Mg^{2+} ions and O atoms, as indicated from the blue dots. The underestimation of vdW repulsion results in a stronger attraction between Mg^{2+} and O atoms, which in turn requires more energy to disrupt the Mg^{2+} -O_α coordination bond. Consequently, this leads to a high TS barrier and higher relative energy for transitioning to the C2 conformation. The root-mean square deviation (RMSD) between the $E^{MM,vdW}$ data calculated from QM-derived LJ parameters and the $E^{QM,vdW}$ is 5.1 kcal/mol, with a Pearson correlation coefficient 0.938. In contrast, the $E^{MM,vdW}$ calculated from

original LJ parameters exhibited an RMSD value of 33.7 kcal/mol compared to $E^{QM,vdW}$ energies.

The orange PMF curve in **Figure 4b** represents the results obtained using default HF charges, the CMAP₃₄, and the QM-derived LJ parameters. Compared to the 5.3 kcal/mol shown in **Figure 3a**, the free energy difference decreased to 0.3 kcal/mol. The Mg²⁺-O_α distance corresponding to the most stable C2 conformation is 4.1 Å, and a respective structure of C2 conformations (RSC₂) extracted from US windows confirms the bidentate coordination of the Mg²⁺ ion with the ATP β-, and γ-O atoms, as illustrated in **Figure 4c**. Additionally, the TS barrier for conformational change in **Figure 4b** also decreased to a reasonable value of 11.1 kcal/mol, compared to 13.8 kcal/mol obtained from the CHARMM27 force field.¹⁴ This simulation demonstrates that fitting force field parameters using precise QM energies can enhance the description of interactions between Mg²⁺ ions and O atoms. However, the orange PMF curve is not entirely satisfactory, since the C2 conformations of ATP·Mg²⁺ complexes are more preferable than C3 conformations, as observed in NMR experiments.

3.5 Polarized Charge Effects on Conformational Equilibrium of ATP·Mg⁺

Another factor affecting the interaction between Mg²⁺ ions and O atoms is the polarization effect of the P and O atoms in ATP. One way to explicitly account for the polarization effect in the vdW interaction is to use the LJ 12-6-4 potential^{11, 44, 45} instead of the 12-6 potential. Alternatively, we could use RESP charges calculated from DFT methods to substitute the original HF charges, since recent studies⁴⁶ have shown that DFT methods such as B3LYP under the PCM model, produce more polarized atomic charges and accurate molecular dipole moments than the HF/6-31G* method.¹⁹ Duan et al.⁴⁷ had used the B3LYP method with the PCM model to calculate atomic charges for developing the AMBER03 force field. Therefore, we aim to use a set of strongly polarized charges calculated to evaluate the electrostatic interactions.

The atomistic RESP charges of ATP (**Table S1** of **SI**) were recalculated using the B3LYP-D3BJ/6-311+G** method with the PCM model to represent the water solution (with a dielectric constant of 78.3). The difference between the HF and B3LYP charges

primarily arises from the heavy atoms. To assess the effect of these polarized charges on simulations, we refitted the dihedral angle parameters for ATP under the B3LYP charges, shown in **Table 1**, and conducted US simulations using the refitted dihedral angles, CMAP₃₄, the QM-derived LJ parameters, and B3LYP charges. The resulting purple PMF curve is presented in **Figure 4b**. Its relative free energy ΔG_{C23} is -0.9 kcal/mol, which is 1.2 kcal/mol lower than that of the yellow curve. The TS barrier is estimated to be 11.3 kcal/mol, similar to the 11.1 kcal/mol of the yellow curve. **Figure 4c** confirms that the corresponding RS_{C2} is indeed bi-coordinated. The results indicate that the purple curve obtained using the B3LYP charges provides a better fit than the yellow ones from HF charges.

Further, we performed 150 ns REMD simulations to sample the C3 and C2 conformations of ATP·Mg²⁺ in solution, and compared to the results of using HF charges. The initial structures for the REMD simulations were based on C3 conformations. Principal component analysis of the backbones of the triphosphate groups in ATP·Mg²⁺ complexes was performed by projecting the REMD trajectories at 300 K on a 2D plot, using the first two major principal components, PC1 and PC2. **Figure 5a** illustrates the REMD-sampled C3 and C2 regions, and the distributions of the complex crystal structures. In contrast, the 150 ns REMD simulation with the original parameters and HF charges only sampled the localized C3 region, as depicted in **Figure 5b**. **Figure 5c** and **Figure 5d** show the representative structures of C3 and C2 conformations (RS_{C3} and RS_{C2}) generated from clustering analysis of the REMD trajectories and crystal structures, respectively. It is evident that the sampled regions closely align with the distributions observed in crystal structures. A comparison of the RS_{C3} and RS_{C2} structures indicates that the REMD simulations using new force field successfully and efficiently sampled both C3 and C2 conformations, despite the high barriers separating them. In addition, we developed the parameters for adenosine diphosphate (ADP) (**Figure S5 of SI**) using B3LYP-derived charges (**Table S2 of SI**).

3.6 Conformational Equilibrium of GTP·Mg²⁺ Complexes

The main difference between ATP and GTP molecules is their bases. To perform accurate MD simulations for GTP·Mg²⁺ complexes, we calculated the B3LYP charges of GTP (**Table S3** of **SI**) and developed the force fields for GTP based on the RTP model. We conducted US simulations and evaluated the corresponding PMF curve for conformational changes, as shown in **Figure 6**. The PMF curve of GTP·Mg²⁺ closely resembles that of ATP·Mg²⁺. The green curve exhibits two local energy minima at Mg²⁺–O_α distances 2.1 and 4.0 Å, with the corresponding structures presented in the inset of **Figure 6**. The estimated free energy difference ΔG₂₃ from the PMF curve is 0.1 kcal/mol. For the GTP·Mg²⁺ complexes, the C3 conformations were preferred to C2 conformations as what has been reported in previous NMR measurements.^{6,48} It should be noted that when GTP·Mg²⁺ is complexed with signaling transduction proteins such as Ras,^{49, 50} GTP·Mg²⁺ usually adopts a bi-coordinated structure rather than a tri-coordinated one due to the environmental constraints within the proteins. Based on the validated results for GTP·Mg²⁺ complexes, we also developed the force field parameters for guanosine diphosphate (GDP) (**Figure S5** of **SI**) molecules using B3LYP-derived polarized charges (**Table S2** of **SI**).

4. Conclusion

In this study, we proposed the RTP model and developed force field parameters for the triphosphate groups in ATP and GTP. We primarily considered several factors influencing the equilibrium distribution of the C3 and C2 conformations. First, we examined the impact of the ribose ring on the conformation changes of the triphosphate group. We recalculated the 1D PES curves for dihedral angles in the RTP model, revealing significant differences from the MTP model. Second, we used CMAP potentials to describe the coupling effects between dihedral angles. Next, we refined the vdW parameters for accurately describing the interactions of Mg²⁺ ions with P and O atoms through high-level DFT calculations. Combining the polarized charges calculated using the B3LYP/6-311+G** method with these new parameters, we obtained a free energy difference ΔG_{C23} of -0.9 kcal/mol, which aligns with the results observed in NMR experiments.

Further simulations demonstrated that the new force field parameters could accurately sample the C3 and C2 conformations of ATP·Mg²⁺. Based on these results, we developed force field parameters for GTP, ADP, and GDP molecules. In future applications, we recommend using the B3LYP-derived polarization charges, along with the calculated 2D-CMAP and QM-derived vdW parameters, to simulate biological systems such as the adenylate kinases,⁵¹ microtubules,^{52, 53} and Ras proteins⁵⁴⁻⁵⁶ that contain the ATP·Mg²⁺, ADP·Mg²⁺, GTP·Mg²⁺ and GDP·Mg²⁺ complexes. The relevant parameter files have been attached.

ASSOCIATED CONTENT

Supporting Information

Figure S1 presents the estimated PMF for ATP·Mg²⁺ complex using original AMBER force fields. **Figure S2** presents the calculated PES curves for dihedral angles using the HF and MP2 methods. **Figure S3** presents fitted results based the RTP model. **Figure S4** shows the calculated CMAP₄₅ and CMAP₅₆. **Figure S5** shows the topology structures of ADP and GDP molecules. **Table S1** presents original HF charges and B3LYP-derived charges for ATP. **Table S2** presents original HF charges and B3LYP-derived charges for ADP and GDP. **Table S3** presents original HF charges and B3LYP-derived charges for atoms for GTP. **Section S1** provides a script for using the new developed parameters.

AUTHOR INFORMATION

Corresponding Authors

*Emails: fxia@chem.ecnu.edu.cn (F.X.)

ORCID

Yuwei Zhang: 0009-0002-8741-3889

Pengfei Li: 0000-0002-2572-5935

Ruibo Wu: 0000-0002-1984-046X

Fei Xia: 0000-0001-9458-9175

ACKNOWLEDGMENT

This work was supported by the National Natural Science Foundation of China (No. 22073029, 22473118). P.L. acknowledges the financial support by the start-up funds from Loyola University Chicago (to P.L.). We also acknowledge the support of the NYU-ECNU Center for Computational Chemistry at NYU Shanghai as well as the ECNU Public Platform for Innovation (001) for providing computer time.

References:

1. Boyer, P. D. Energy, Life, and ATP (Nobel Lecture). *Angew. Chem. Int. Ed.* **1998**, *37* (17), 2296-2307.
2. Kolch, W.; Berta, D.; Rosta, E. Dynamic Regulation of RAS and RAS Signaling. *Biochem. J.* **2023**, *480* (1), 1-23.
3. Li, P.; Merz, K. M., Jr. Metal Ion Modeling Using Classical Mechanics. *Chem. Rev.* **2017**, *117* (3), 1564-1686.
4. Li, P.; Song, L. F.; Merz, K. M., Jr. Systematic Parameterization of Monovalent Ions Employing the Nonbonded Model. *J. Chem. Theory Comput.* **2015**, *11* (4), 1645-57.
5. Huang, S. L.; Tsai, M.-D. Does the Magnesium(II) Ion Interact with the γ -Phosphate of Adenosine. *Biochemistry* **1982**, *21* (5), 951-959.
6. Takeuchi, H.; Murata, H.; Harada, I. Interaction of Adenosine 5'-Triphosphate with Mg²⁺ Vibrational Study of Coordination Sites by Use of ¹⁸O-Labeled. *J. Am. Chem. Soc.* **1988**, *91* (5), 1629-1637.
7. Weiner, S. J.; Kollman, P. A.; Case, D. A.; Singh, U. C.; Ghio, C.; Alagona, G.; Profeta, J., S.; Weiner, P. A New Force Field for Molecular Mechanical Simulation of Nucleic Acids and Proteins. *J. Am. Chem. Soc.* **1984**, *106* (3), 765-784.
8. Cornell, W. D.; Cieplak, P.; Bayly, C. I.; Gould, I. R.; Merz, J., K. M.; Ferguson, D. M.; Spellmeyer, D. C.; Fox, T.; Caldwell, J. W.; Kollman, P. A. A Second Generation Force Field for the Simulation of Proteins, Nucleic Acids and Organic Molecules. *J. Am. Chem. Soc.* **1995**, *117* (19), 5179-5197.
9. Pavelites, J. J.; Gao, J. A Molecular Mechanics Force Field for NAD⁺, NADH, and the Pyrophosphate. *J. Comput. Chem.* **1997**, *18* (2), 221-239.
10. Petrova, P.; Koca, J.; Imberty, A. Potential Energy Hypersurfaces of Nucleotide Sugars: Ab Initio Calculations, Force-Field Parametrization, and Exploration of the Flexibility. *J. Am. Chem. Soc.* **1999**, *121* (23), 5535-5547.
11. Koca Findik, B.; Jafari, M.; Song, L. F.; Li, Z.; Aviyente, V.; Merz, K. M., Jr. Binding of Phosphate Species to Ca(2+) and Mg(2+) in Aqueous Solution. *J. Chem.*

Theory Comput. **2024**.

12. Meagher, K. L.; Redman, L. T.; Carlson, H. A. Development of Polyphosphate Parameters for Use with the AMBER Force Field. *J. Comput. Chem.* **2003**, *24* (9), 1016–1025.
13. Buelens, F. P.; Leonov, H.; de Groot, B. L.; Grubmuller, H. ATP-Magnesium Coordination: Protein Structure-Based Force Field Evaluation and Corrections. *J. Chem. Theory Comput.* **2021**, *17* (3), 1922–1930.
14. Branduardi, D.; Marinelli, F.; Faraldo-Gomez, J. D. Atomic-resolution Dissection of the Energetics and Mechanism of Isomerization of Hydrated ATP-Mg(2+) through the SOMA String Method. *J. Comput. Chem.* **2016**, *37* (6), 575–86.
15. Komuro, Y.; Re, S.; Kobayashi, C.; Muneyuki, E.; Sugita, Y. CHARMM Force-Fields with Modified Polyphosphate Parameters Allow Stable Simulation of the ATP-Bound Structure of Ca(2+)-ATPase. *J. Chem. Theory Comput.* **2014**, *10* (9), 4133–42.
16. Mackerell, A. D., Jr.; Feig, M.; Brooks, I., C. L. Extending the Treatment of Backbone Energetics in Protein Force Fields: Limitations of Gas-phase Quantum Mechanics in Reproducing Protein Conformational Distributions in Molecular Dynamics Simulations. *J. Comput. Chem.* **2004**, *25* (11), 1400–15.
17. MacKerell, J., A. D.; Feig, M.; Brooks, I., C. L. Improved Treatment of the Protein Backbone in Empirical Force Fields. *J. Am. Chem. Soc.* **2004**, *126* (3), 698–699.
18. Tian, C.; Kasavajhala, K.; Belfon, K. A. A.; Raguette, L.; Huang, H.; Migués, A. N.; Bickel, J.; Wang, Y.; Pincay, J.; Wu, Q.; Simmerling, C. ff19SB: Amino-Acid-Specific Protein Backbone Parameters Trained against Quantum Mechanics Energy Surfaces in Solution. *J. Chem. Theory Comput.* **2020**, *16* (1), 528–552.
19. Wang, J.; Cieplak, P.; Kollman, P. A. How Well Does a Restrained Electrostatic Potential (RESP) Model Perform in Calculating Conformational Energies of Organic and Biological Molecules? *J. Comput. Chem.* **2000**, *21* (12), 1049–1074.
20. Jeziorski, B.; Moszynski, R.; Szalewicz, K. Perturbation Theory Approach to Intermolecular Potential Energy Surfaces of van der Waals Complexes. *Chem. Rev.*

1994, 94 (7), 1887-1930.

21. Stasyuk, O. A.; Sedlak, R.; Guerra, C. F.; Hobza, P. Comparison of the DFT-SAPT and Canonical EDA Schemes for the Energy Decomposition of Various Types of Noncovalent Interactions. *J. Chem. Theory Comput.* **2018**, 14 (7), 3440-3450.

22. Gaussian 16, Revision C.01, Frisch, M. J.; Trucks, G. W.; Schlegel, H. B.; Scuseria, G. E.; Robb, M. A.; Cheeseman, J. R.; Scalmani, G.; Barone, V.; Petersson, G. A.; Nakatsuji, H.; Li, X.; Caricato, M.; Marenich, A. V.; Bloino, J.; Janesko, B. G.; Gomperts, R.; Mennucci, B.; Hratchian, H. P.; Ortiz, J. V.; Izmaylov, A. F.; Sonnenberg, J. L.; Williams-Young, D.; Ding, F.; Lipparini, F.; Egidi, F.; Goings, J.; Peng, B.; Petrone, A.; Henderson, T.; Ranasinghe, D.; Zakrzewski, V. G.; Gao, J.; Rega, N.; Zheng, G.; Liang, W.; Hada, M.; Ehara, M.; Toyota, K.; Fukuda, R.; Hasegawa, J.; Ishida, M.; Nakajima, T.; Honda, Y.; Kitao, O.; Nakai, H.; Vreven, T.; Throssell, K.; Montgomery, J. A., Jr.; Peralta, J. E.; Ogliaro, F.; Bearpark, M. J.; Heyd, J. J.; Brothers, E. N.; Kudin, K. N.; Staroverov, V. N.; Keith, T. A.; Kobayashi, R.; Normand, J.; Raghavachari, K.; Rendell, A. P.; Burant, J. C.; Iyengar, S. S.; Tomasi, J.; Cossi, M.; Millam, J. M.; Klene, M.; Adamo, C.; Cammi, R.; Ochterski, J. W.; Martin, R. L.; Morokuma, K.; Farkas, O.; Foresman, J. B.; Fox, D. J. Gaussian, Inc., Wallingford CT, 2016.

23. Betz, R. M.; Walker, R. C. Paramfit: Automated Optimization of Force Field Parameters for Molecular Dynamics Simulations. *J. Comput. Chem.* **2015**, 36 (2), 79-87.

24. Case, D. A.; Cheatham, T. E., 3rd; Darden, T.; Gohlke, H.; Luo, R.; Merz, K. M., Jr.; Onufriev, A.; Simmerling, C.; Wang, B.; Woods, R. J. The Amber Biomolecular Simulation Programs. *J. Comput. Chem.* **2005**, 26 (16), 1668-88.

25. Schwerdtfeger, P.; Wales, D. J. 100 Years of the Lennard-Jones Potential. *J. Chem. Theory Comput.* **2024**, 20 (9), 3379-3405.

26. Liu, C.; Piquemal, J.-P.; Ren, P. AMOEBA+ Classical Potential for Modeling Molecular Interactions. *J. Chem. Theory Comput.* **2019**, 15 (7), 4122-4139.

27. Lu, T.; Chen, Q. Simple, Efficient, and Universal Energy Decomposition Analysis Method Based on Dispersion-Corrected Density Functional Theory. *J. Phys. Chem. A*

2023, *127* (33), 7023-7035.

28. Becke, A. D. Density-functional Exchange-energy Approximation with Correct Asymptotic Behavior. *Phys. Rev. A* **1988**, *38* (6), 3098-3100.

29. Lee, C.; Yang, W.; Parr, R. G. Development of the Colle-Salvetti Correlation-energy Formula into a Functional of the Electron Density. *Phys. Rev. B* **1988**, *37* (2), 785-789.

30. Grimme, S.; Ehrlich, S.; Goerigk, L. Effect of the Damping Function in Dispersion Corrected Density Functional Theory. *J. Comput. Chem.* **2011**, *32* (7), 1456-65.

31. Torrie, G. M.; Valleau, J. P. Nonphysical Sampling Distributions in Monte Carlo Free-energy Estimation: Umbrella Sampling. *J. Comput. Phys.* **1977**, *23* (2), 187-199.

32. Tomasi, J.; Mennucci, B.; Cammi, R. Quantum Mechanical Continuum Solvation Models. *Chem. Rev.* **2005**, *105* (8), 2999-3093.

33. Brown, N. R.; Noble, M. E. M.; Lawrie, A. M.; Morris, M. C.; Tunnah, P.; Divita, G.; Johnson, L. N.; Endicott, J. A. Effects of Phosphorylation of Threonine 160 on Cyclin-dependent Kinase 2 Structure and Activity. *J. Biol. Chem.* **1999**, *274* (13), 8746-8756.

34. Jorgensen, W. L.; Chandrasekhar, J.; Madura, J. D.; Impey, R. W.; Klein, M. L. Comparison of Simple Potential Functions for Simulating Liquid Water. *J. Chem. Phys.* **1983**, *79* (2), 926-935.

35. Li, P.; Roberts, B. P.; Chakravorty, D. K.; Merz, K. M., Jr. Rational Design of Particle Mesh Ewald Compatible Lennard-Jones Parameters for +2 Metal Cations in Explicit Solvent. *J. Chem. Theory Comput.* **2013**, *9* (6), 2733-2748.

36. Ryckaert, J. P.; Ciccotti, G.; Berendsen, H. J. C. Numerical Integration of a System with Constraints: of the Cartesian Equations of Motion Molecular Dynamics of n-Alkanes. *J. Comput. Phys.* **1977**, *23* (3), 321-341.

37. Salomon-Ferrer, R.; Gotz, A. W.; Poole, D.; Le Grand, S.; Walker, R. C. Routine Microsecond Molecular Dynamics Simulations with AMBER on GPUs. 2. Explicit Solvent Particle Mesh Ewald. *J. Chem. Theory Comput.* **2013**, *9* (9), 3878-88.

38. Pastor, R. W.; Brooks, B. R.; Szabo, A. An Analysis of the Accuracy of Langevin

- and Molecular Dynamics Algorithms. *Mol. Phys.* **1988**, *65* (6), 1409-1419.
39. Berendsen, H. J. C.; Postma, J. P. M.; van Gunsteren, W. F.; DiNola, A.; Haak, J. R. Molecular Dynamics with Coupling to an External Bath. *J. Chem. Phys.* **1984**, *81* (8), 3684-3690.
40. Maier, J. A.; Martinez, C.; Kasavajhala, K.; Wickstrom, L.; Hauser, K. E.; Simmerling, C. ff14SB: Improving the Accuracy of Protein Side Chain and Backbone Parameters from ff99SB. *J. Chem. Theory Comput.* **2015**, *11* (8), 3696-3713.
41. Kumar, S.; Rosenberg, J. M.; Bouzida, D.; Swendsen, R. H.; Kollman, P. A. The Weighted Histogram Analysis Method for Free - energy Calculations on Biomolecules. I. The Method. *J. Comput. Chem.* **2004**, *13* (8), 1011-1021.
42. Sugita, Y.; Okamoto, Y. Replica-exchange Molecular Dynamics Method for Protein Folding. *Chem. Phys. Lett.* **1999**, *314* (1-2), 141-151.
43. Roe, D. R.; Cheatham, T. E. PTRAJ and CPPTRAJ: Software for Processing and Analysis of Molecular Dynamics Trajectory Data. *J. Chem. Theory Comput.* **2013**, *9* (7), 3084-3095.
44. Li, P.; Song, L. F.; Merz, K. M., Jr. Parameterization of Highly Charged Metal Ions Using the 12-6-4 LJ-type Nonbonded Model in Explicit Water. *J. Phys. Chem. B* **2015**, *119* (3), 883-895.
45. Li, Z.; Bhowmik, S.; Sagresti, L.; Brancato, G.; Smith, M.; Benson, D. E.; Li, P.; Merz, K. M., Jr. Simulating Metal-Imidazole Complexes. *J. Chem. Theory Comput.* **2024**, *20* (15), 6706-6716.
46. Zhou, A.; Schaperl, M.; Nerenberg, P. S. Benchmarking Electronic Structure Methods for Accurate Fixed-Charge Electrostatic Models. *J. Chem. Inf. Model.* **2020**, *60* (1), 249-258.
47. Duan, Y.; Wu, C.; Chowdhury, S.; Lee, M. C.; Xiong, G.; Zhang, W.; Yang, R.; Cieplak, P.; Luo, R.; Lee, T.; Caldwell, J.; Wang, J.; Kollman, P. A Point-Charge Force Field for Molecular Mechanics Simulations of Proteins based on Condensed-phase Quantum Mechanical Calculations. *J. Comput. Chem.* **2003**, *24* (16), 1999-2012.

48. Wang, J. H.; Xiao, D. G.; Deng, H.; Callender, R.; Webb, M. R. Vibrational Study of Phosphate Modes in GDP and GTP and their Interaction with Magnesium in Aqueous Solution. *Biospectroscopy* **1998**, *4* (4), 219-227.
49. Spoerner, M.; Hozsa, C.; Poetzl, J. A.; Reiss, K.; Ganser, P.; Geyer, M.; Kalbitzer, H. R. Conformational States of Human Rat sarcoma (Ras) Protein Complexed with its Natural Ligand GTP and Their Role for Effector Interaction and GTP Hydrolysis. *J. Biol. Chem.* **2010**, *285* (51), 39768-78.
50. Rudack, T.; Xia, F.; Schlitter, J.; Kotting, C.; Gerwert, K. Ras and GTPase-activating Protein (GAP) Drive GTP into a Precatalytic State as Revealed by Combining FTIR and Biomolecular Simulations. *Proc. Natl. Acad. Sci. U.S.A.* **2012**, *109* (38), 15295-300.
51. Zhang, Y.; Cao, Z.; Zhang, J. Z.; Xia, F. Double-Well Ultra-Coarse-Grained Model to Describe Protein Conformational Transitions. *J. Chem. Theory Comput.* **2020**, *16* (10), 6678-6689.
52. Zha, J.; Zhang, Y.; Xia, K.; Grater, F.; Xia, F. Coarse-Grained Simulation of Mechanical Properties of Single Microtubules With Micrometer Length. *Front. Mol. Biosci.* **2020**, *7*, 632122.
53. Zha, J.; Xia, F. Developing Hybrid All-Atom and Ultra-Coarse-Grained Models to Investigate Taxol-Binding and Dynein Interactions on Microtubules. *J. Chem. Theory Comput.* **2023**, *19* (16), 5621-5632.
54. Zeng, J.; Weng, J.; Zhang, Y.; Xia, F.; Cui, Q.; Xu, X. Conformational Features of Ras: Key Hydrogen-Bonding Interactions of Gln61 in the Intermediate State during GTP Hydrolysis. *J. Phys. Chem. B* **2021**, *125* (31), 8805-8813.
55. Zeng, J.; Chen, J.; Xia, F.; Cui, Q.; Deng, X.; Xu, X. Identification of Functional Substates of KRas during GTP Hydrolysis with Enhanced Sampling Simulations. *Phys. Chem. Chem. Phys.* **2022**, *24* (13), 7653-7665.
56. Hu, F.; Wang, Y.; Zeng, J.; Deng, X.; Xia, F.; Xu, X. Unveiling the State Transition Mechanisms of Ras Proteins through Enhanced Sampling and QM/MM Simulations. *J. Phys. Chem. B* **2024**, *128* (6), 1418-1427.

Table 1. The angle and dihedral parameters of the RTP models are derived by fitting the potential energy curves of the dihedral angles shown in **Figure 1** using the HF/6-31+G* method and B3LYP-D3BJ/6-311+G** method with the PCM model, respectively. For the dihedral angles, $V_n/2$ represents the magnitude of the torsions in kcal/mol, γ denotes the phase offset in degrees, and n indicates the periodicity. The K_θ and θ represent the force constant and equilibrium value of the P-O-P angle, respectively.

Models	MTP					RTP				RTP			
Methods	HF/6-31G*					HF/6-31G*				B3LYP-D3BJ/6-311+G**			
No.	Dihedrals	$V_n/2$	γ	n	Dihedrals	$V_n/2$	γ	n	Dihedrals	$V_n/2$	γ	n	
1	P-OS-P-O3	0.085	0	3	P-OS-P-O3	0.197	-18.92	3	P-OS-P-O3	0.095	51.52	3	
2	P-OS-P-O2	0.355	0	2	P-OS-P-O2	0.204	103.11	2	P-OS-P-O2	-0.076	30.39	2	
3	P-OS-P-OS	0.897	0	1	P-OS-P-OS	2.867	-18.72	1	P-OS-P-OS	-0.824	92.24	1	
					P-OS-P-OY	0.796	8.48	1	P-OS-P-OY	1.708	13.88	1	
4	CT-OS-P-O2	-0.406	0	2	CT-OY-P-O2	-1.193	68.39	2	CT-OY-P-O2	-0.020	92.87	2	
		0.590	0	3		-0.308	150.63	3		-0.211	107.08	3	
5	CT-OS-P-OS	-1.560	0	1	CT-OY-P-OS	-2.577	121.18	1	CT-OY-P-OS	1.400	51.75	1	
6	HC-CT-OS-P	0.035	0	3	H1-CT-OY-P	1.401	164.87	3	H1-CT-OY-P	-0.896	-15.97	3	
	<i>Angle</i>	K_θ	θ		<i>Angle</i>	K_θ	θ		<i>Angle</i>	K_θ	θ		
7	P-OS-P	12.685	150.0		P-OS-P	20.117	142.9		P-OS-P	56.45	142.9		

Table 2. Comparison of the original LJ parameters A_{ij} and B_{ij} calculated from Ref.12 with the QM-derived ones using the B3LYP-D3BJ/6-31+G* method for the pairwise interactions of Mg^{2+} ions and P, O atom types. The units of A_{ij} and B_{ij} are $\text{kcal}\cdot\text{\AA}^{12}/\text{mol}$ and $\text{kcal}\cdot\text{\AA}^6/\text{mol}$, respectively. The parameters are the same for both O3 and O2 atom types, as well as OS and OY.

Atom Type Pair	$\text{Mg}^{2+}\text{--O3/O2}$	$\text{Mg}^{2+}\text{--OS/OY}$	$\text{Mg}^{2+}\text{--P}$
Original A_{ij}	26767.87	26326.74	132977.70
QM-derived A_{ij}	56958.78	26407.56	133097.78
Original B_{ij}	70.40	66.22	155.01
QM-derived B_{ij}	69.26	66.18	154.94

Figure 1 An illustration of the tridentate (C3) or bidentate (C2) conformations of ATP·Mg²⁺ or GTP·Mg²⁺ complexes. For both the MTP and ATP models, the left structures are labeled with atomic names, while the right cartoons depict the corresponding atomic types.

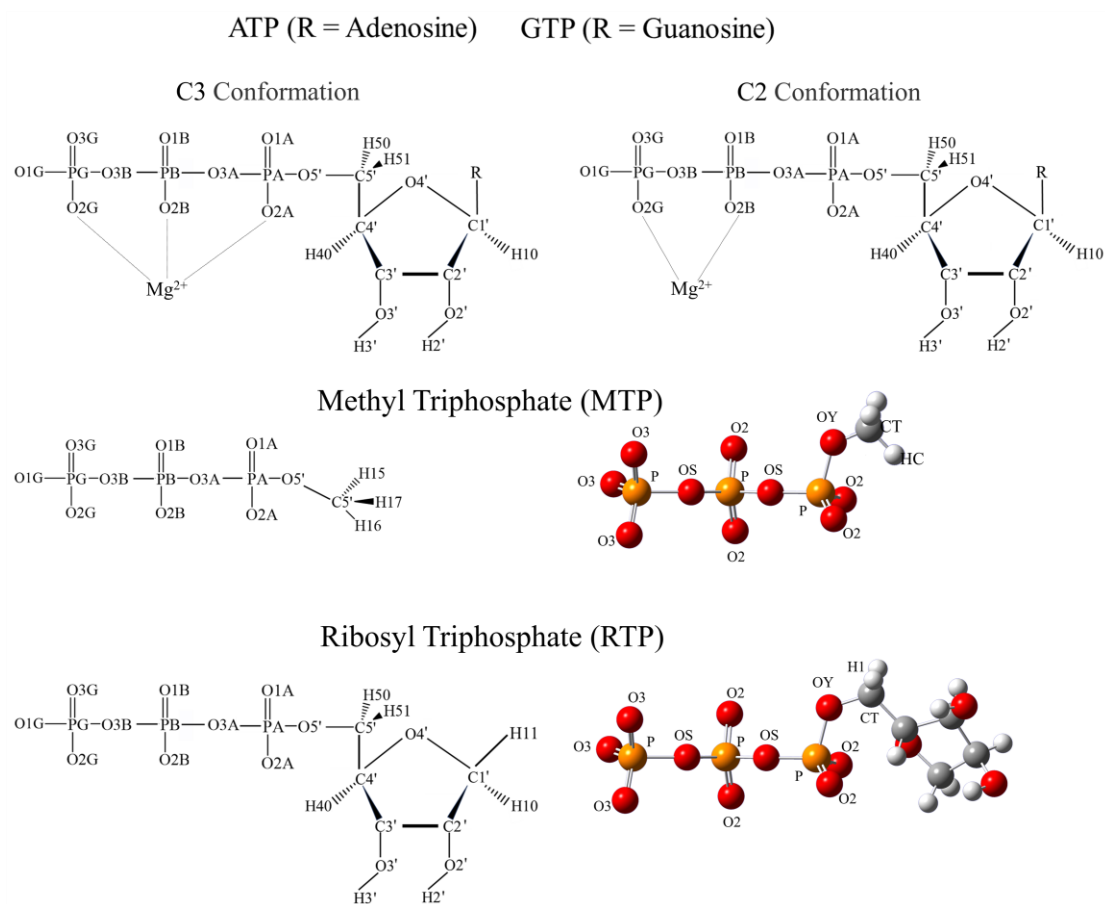


Figure 2. Calculated potential energy curves for the dihedrals O1G-PG-O3B-PB, PG-O3B-PB-O3A, O3B-PB-O3A-PA, PB-O3A-PA-O5', O3A-PA-O5'-C5', and PA-O5'-C5'-C4', respectively. The black curves represent the results for the MTP model, while the red curves represent the results for the RTP models. Dihedral angles in the MTP and RTP models were scanned at 10-degree and 15-degree intervals, respectively, using the HF/6-31+G* method. Energy units are given in kcal/mol.

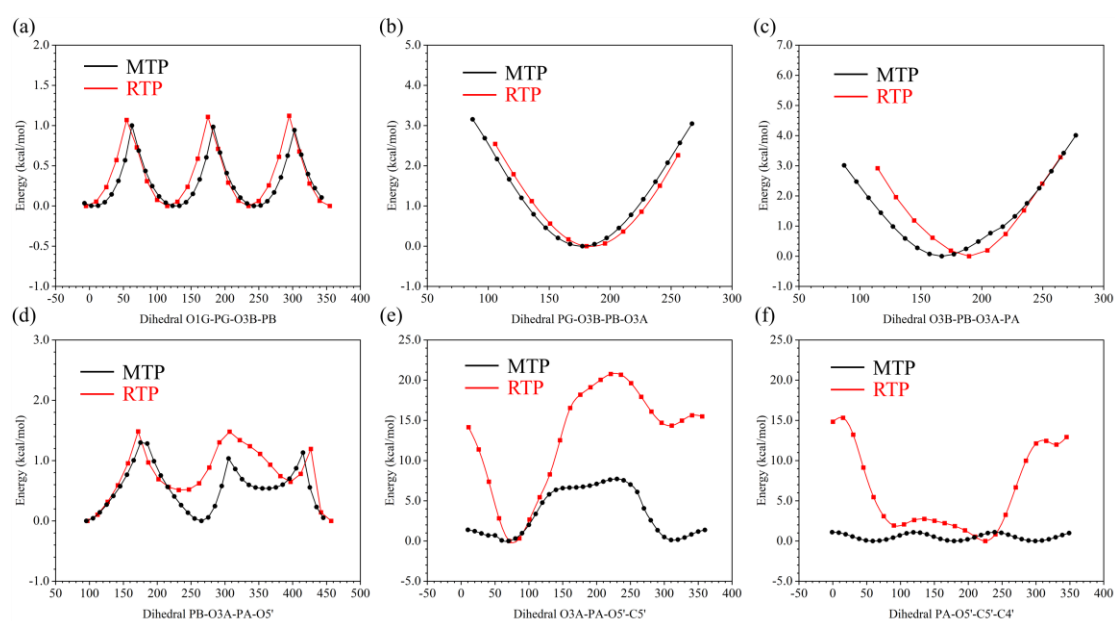


Figure 3. (a) The calculated PMF curves for the transition of ATP·Mg²⁺ complexes from the C3 to C2 conformations obtained using US simulations. Error bars represent standard deviations. The reaction coordinate Mg²⁺-O_α distance ranges from 1.7 to 5.9 Å and is divided into 43 windows. The black curve shows the results of the MTP model, while the red and blue curves correspond to the RTP models without and with CMAP₃₄ corrections, respectively. The Mg²⁺-O_α distances and relative energies of the C3, TS, and C2 conformations are given in parentheses. Hollow triangles indicate the local minima within the C2 regions. (b) Histogram shows the distribution of Mg²⁺-O_α distances, based on 1685 ATP·Mg²⁺ complexes extracted from crystal structures which includes 1142 C2 and 519 C3 conformations. The distributions are fitted with Gaussian functions, as indicated by the dashed line. (c) The 2D CMAP₃₄ calculated using the HF/6-31+G* method, plotted for the PB-O3A-PA-O5' and O3B-PB-O3A-PA dihedrals.

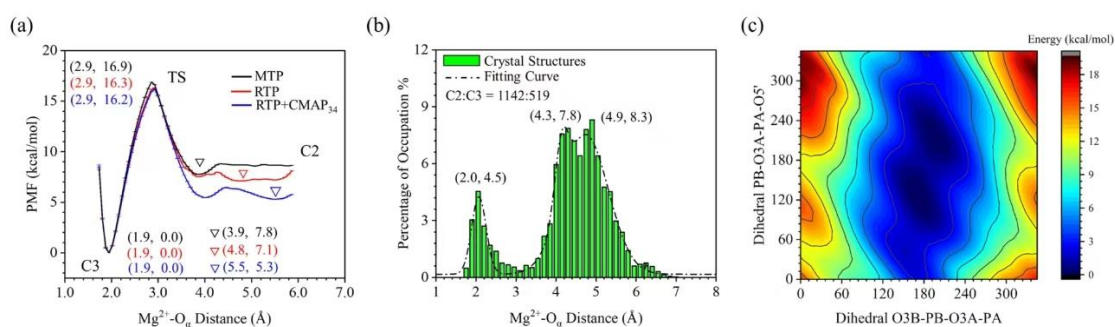


Figure 4. (a) A comparison of $E^{QM,vdW}$ obtained from DFT calculations and $E^{MM,vdW}$ calculated from force fields. The blue dots and red triangles denote the MM vdW results calculated using the original and new QM-derived LJ parameters, respectively. The RMSD values of the blue and red MM results compared to $E^{QM,vdW}$ are 33.7 and 5.1 kcal/mol, respectively. (b) The calculated PMF curves for the ATP·Mg²⁺ complexes transitioning from the C3 to C2 conformations using US simulations are depicted, with error bars representing standard deviations. The black and blue curves correspond to the RTP model with the original force fields and the QM-derived vdW parameters, respectively. The Mg²⁺-O_α distances and relative energies of the C3, TS, and C2 conformations are indicated in parentheses. (c) The representative structures of C2 conformations (RS_{C2}) correspond to the PMF minima shown in plot (b).

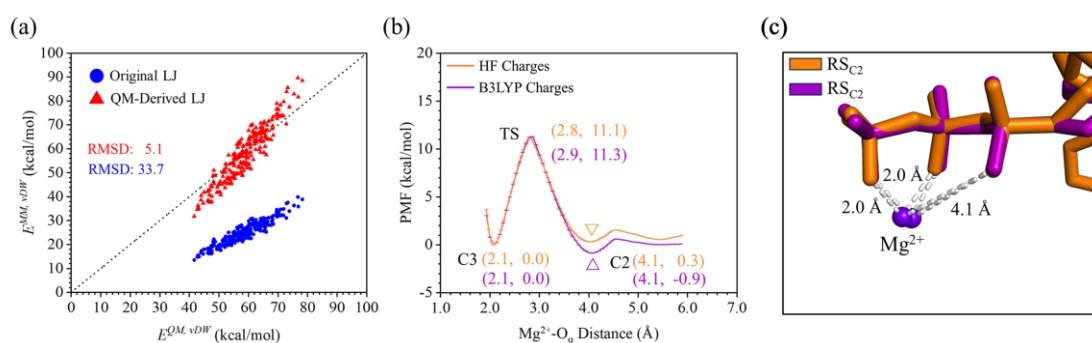


Figure 5. (a) The constructed 2D-FEL for ATP·Mg²⁺ transitioning from the C3 to the C2 based on REMD simulations using the B3LYP-derived charges and parameters. The two energy basins represent the distributions of the C3 and C2 conformations. The scattered circles represent the projections of crystal structures for ATP·Mg²⁺ complexes on the 2D-FEL. (b) The constructed 2D-FEL from REMD simulations using the original HF charges and parameters. A comparison of the (c) C3 and (d) C2 representative structures (RS_{C3} and RS_{C2}) extracted from REMD simulations with those from crystal structures.

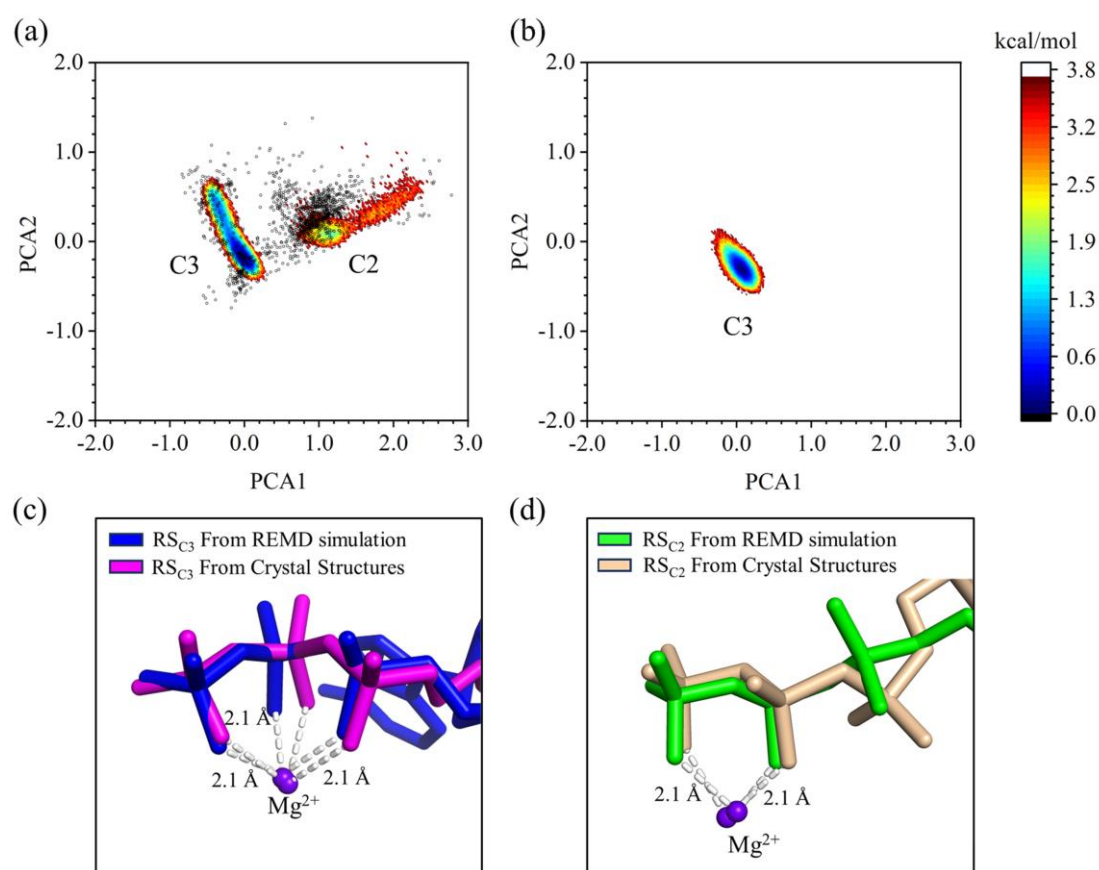
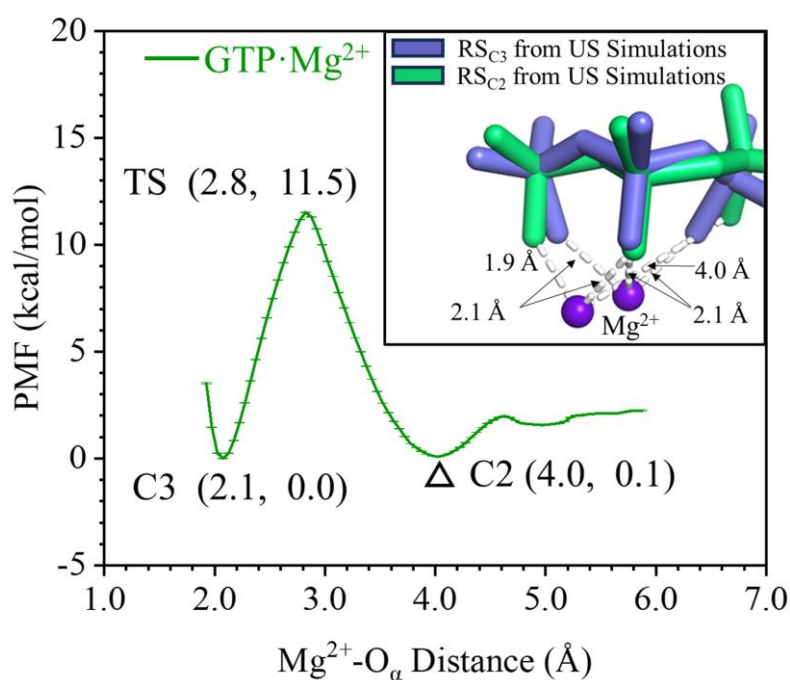


Figure 6. The calculated PMF curves for the transition of GTP·Mg²⁺ complexes from the C3 to C2 conformations obtained using US simulations with the B3LYP-derived charges and parameters. Error bars represent standard deviations. The Mg²⁺-O_α distances and relative energies of the C3, TS, and C2 conformations are given in parentheses. The calculated TS barrier and the free energy difference are 11.5 kcal/mol and 0.1 kcal/mol, respectively. The insert shows a comparison of the C3 and C2 representative structures (RS_{C3} and RS_{C2}) extracted from the two minima in the PMF curve.



Supporting Information

Figure S1. The 1D-PMF for the conformational change from the C3 to C2 structures of the ATP·Mg²⁺ complex was estimated based on the US simulations using AMBER force fields according to the Mg²⁺-O_α distance.

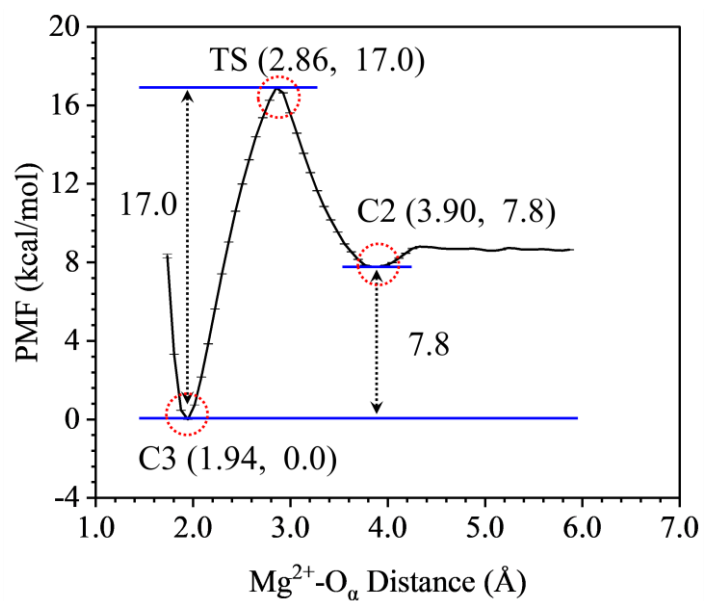


Figure S2. Calculated potential energy curves for the dihedral types O3-P-OS-P, P-OS-P-OS, P-OS-P-OS, P-OS-P-OS, OS-P-OS-CT, and OS-P-CT-H1, respectively. The black curves represent the calculated results using the MP2/6-31+G* method, while the red curves represent the ones using the HF/6-31+G* method. Dihedral angles were scanned at 10-degree intervals and energy units are given in kcal/mol.

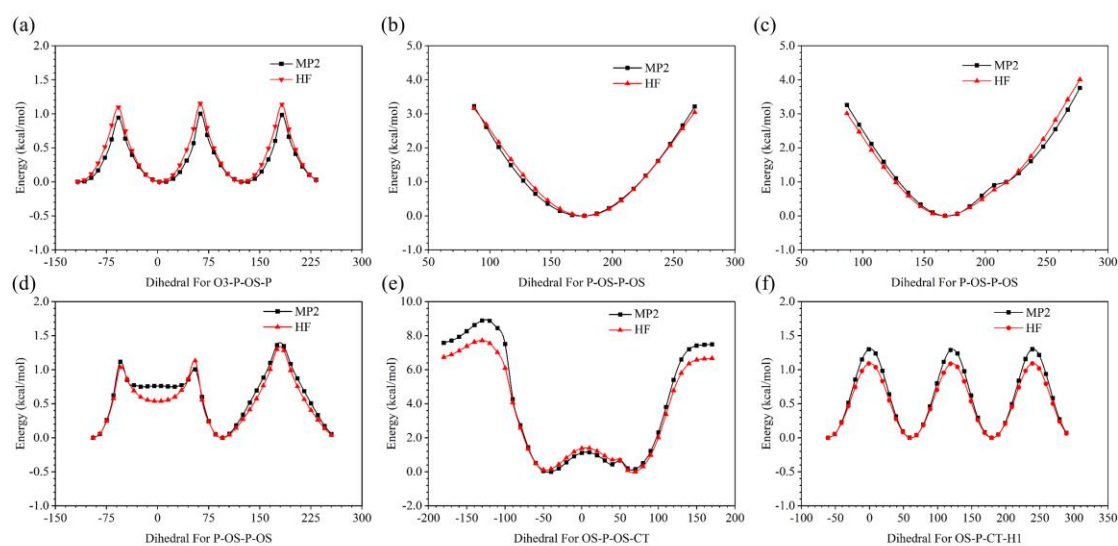


Figure S3. Comparison of the potential energy curves for the dihedrals O1G-PG-O3B-PB, PG-O3B-PB-O3A, O3B-PB-O3A-PA, PB-O3A-PA-O5', O3A-PA-O5'-C5', and PA-O5'-C5'-C4'. The black, red, and blue curves represent the results of the MTP model, the RTP model, and the fitted results using *paramfit*, respectively. The average RMSD value of the fitted data compared to the RTP model is 1.46 kcal/mol.

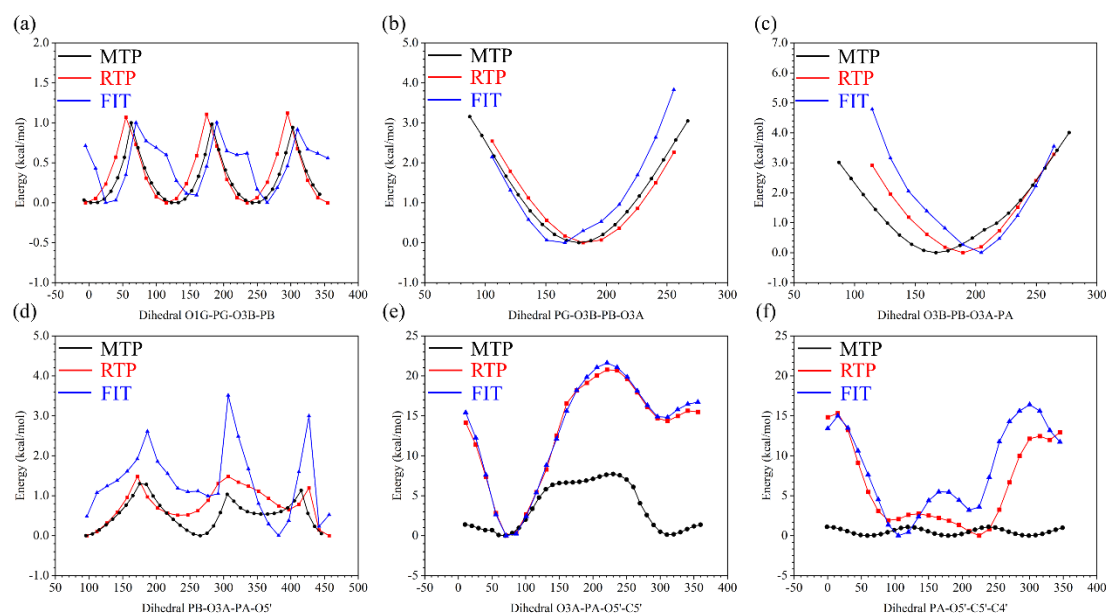


Figure S4. The incomplete 2D (a) CMAP₄₅ and CMAP₅₆ calculated using the HF/6-31+G* method.

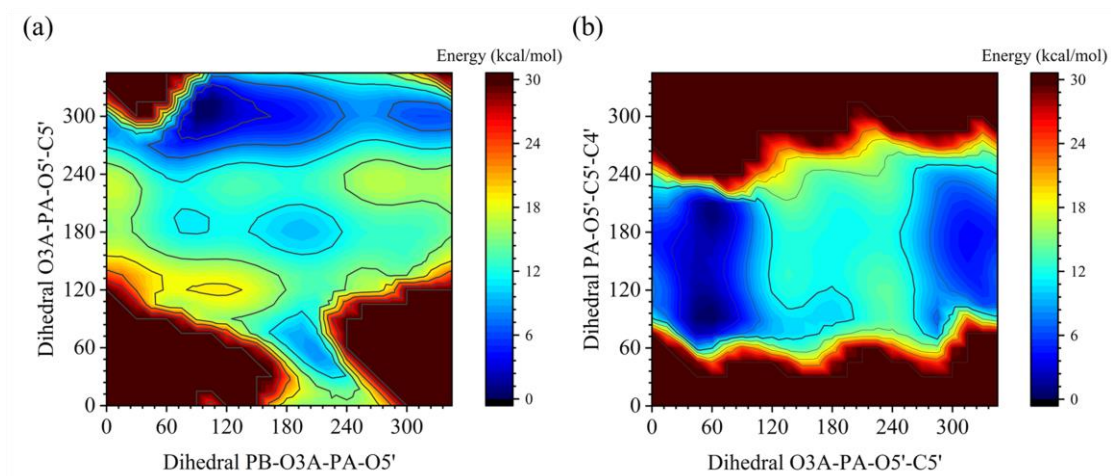


Figure S5. A schematic illustration of the topology structures of ADP and GDP.

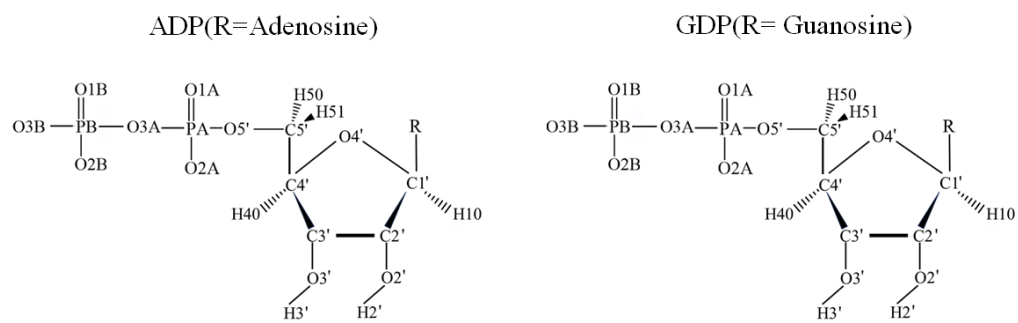


Table S1. Comparison of atomic charges in ATP obtained by RESP fitting from electrostatic potentials calculated using HF/6-31G* and B3LYP-D3BJ/6-311+G** in PCM.

Atom Names	HF Charges	B3LYP Charges		HF Charges	B3LYP Charges
O1G	-0.9526	-1.0327	C8	0.2006	0.3579
PG	1.2650	1.5524	H80	0.1553	0.1108
O2G	-0.9526	-1.0327	N7	-0.6073	-0.7078
O3G	-0.9526	-1.0327	C5	0.0515	0.0693
O3B	-0.5322	-0.6957	C6	0.7009	0.7878
PB	1.3852	1.5528	N6	-0.9019	-0.9445
O1B	-0.8894	-0.9506	H60	0.4115	0.4370
O2B	-0.8894	-0.9506	H61	0.4115	0.4370
O3A	-0.5689	-0.6819	N1	-0.7615	0.8172
PA	1.2532	1.4253	C2	0.5875	0.5309
O1A	-0.8799	-0.9041	H2	0.0473	0.0634
O2A	-0.8799	-0.9041	N3	-0.6997	-0.6838
O5'	-0.5987	-0.5669	C4	0.3053	0.4197
C5'	0.0558	-0.0142	C3'	0.2022	0.2676
H50	0.0679	0.0880	H30	0.0615	0.0867
H51	0.0679	0.0880	O3'	-0.6541	-0.7597
C4'	0.1065	0.2628	H3'	0.4376	0.4733
H40	0.1174	0.1052	C2'	0.0670	0.0740
O4'	-0.3548	-0.5296	H20	0.0972	0.1178
C1'	0.0394	0.3132	O2'	-0.6139	-0.7100
H10	0.2007	0.0994	H2'	0.4186	0.4277
N9	-0.0251	-0.2293			

Table S2. Comparison of atomic charges in ADP and GDP obtained by RESP fitting from electrostatic potentials calculated using HF/6-31G* and B3LYP-D3BJ/6-311+G** in PCM.

GDP	HF Charges	B3LYP Charges	ADP	HF Charges	B3LYP Charges
O1B	-0.9552	-1.0296	O1B	-0.9552	-1.0293
PB	1.3672	1.5494	PB	1.3672	1.5490
O2B	-0.9552	-1.0296	O2B	-0.9552	-1.0293
O3B	-0.9552	-1.0296	O3B	-0.9552	-1.0293
O3A	-0.6346	-0.6950	O3A	-0.6346	-0.6966
PA	1.4929	1.5567	PA	1.4929	1.5402
O1A	-0.9474	-0.9500	O1A	-0.9474	-0.9462
O2A	-0.9474	-0.9500	O2A	-0.9474	-0.9462
O5'	-0.6579	-0.6559	O5'	-0.6579	-0.6410
C5'	0.0558	0.0269	C5'	0.0558	0.0166
H50	0.0679	0.0657	H50	0.0679	0.0685
H51	0.0679	0.0657	H51	0.0679	0.0685
C4'	0.1065	0.3317	C4'	0.1065	0.3644
H40	0.1174	0.0864	H40	0.1174	0.0780
O4'	-0.3548	-0.5563	O4'	-0.3548	-0.5584
C1'	0.0191	0.2758	C1'	0.0394	0.2990
H10	0.2006	0.1004	H10	0.2007	0.1052
N9	0.0492	-0.0819	N9	-0.0251	-0.2061
C8	0.1374	0.2886	C8	0.2006	0.3298
H80	0.1640	0.1189	H80	0.1553	0.1230
N7	-0.5709	-0.7268	N7	-0.6073	-0.7043
C5	0.1744	0.2022	C5	0.0515	0.0875
C6	0.4770	0.6161	C6	0.7009	0.7767
O6	-0.5597	-0.6604	N6	-0.9019	-0.9410
N1	-0.4787	-0.6322	H60	0.4115	0.4366
H1N	0.3424	0.4171	H61	0.4115	0.4366
C2	0.7657	0.7860	N1	-0.7615	-0.8151
N2	-0.9672	-0.8896	C2	0.5875	0.5326
H21	0.4364	0.4273	H2	0.0473	0.0626
H22	0.4364	0.4273	N3	-0.6997	-0.6766
N3	-0.6323	-0.6484	C4	0.3053	0.3996
C4	0.1222	0.1937	C3'	0.2022	0.2491
C3'	0.2022	0.2859	H30	0.0615	0.0856
H30	0.0615	0.0749	O3'	-0.6541	-0.7687
C2'	0.0670	0.0729	H3'	0.4376	0.4757
H20	0.0972	0.1260	C2'	0.0670	0.0670

GDP	HF Charges	B3LYP Charges	ADP	HF Charges	B3LYP Charges
O2'	-0.6139	-0.7307	H20	0.0972	0.1172
H2'	0.4186	0.4640	O2'	-0.6139	-0.7047
O3'	-0.6541	-0.7724	H2'	0.4186	0.4239
H3'	0.4376	0.4784			

Table S2. Comparison of atomic charges in GTP obtained by RESP fitting from electrostatic potentials calculated using HF/6-31G* and B3LYP-D3BJ/6-311+G** in PCM.

Atom Names	HF Charges	B3LYP Charges		HF Charges	B3LYP Charges
O1G	-0.9526	-1.0314	C8	0.1374	0.2926
PG	1.2650	1.5503	H8	0.1640	0.1180
O2G	-0.9526	-1.0314	N7	-0.5709	-0.7442
O3G	-0.9526	-1.0314	C5	0.1744	0.1961
O3B	-0.5322	-0.6994	C6	0.4770	0.6178
PB	1.3852	1.5575	O6	-0.5597	-0.6613
O1B	-0.8894	-0.9517	N1	-0.4787	-0.6344
O2B	-0.8894	-0.9517	H1	0.3424	0.4180
O3A	-0.5689	-0.6812	C2	0.7657	0.7883
PA	1.2532	1.4246	N2	-0.9672	-0.8876
O1A	-0.8799	-0.9040	H21	0.4364	0.4262
O2A	-0.8799	-0.9040	H22	0.4364	0.4262
O5'	-0.5987	-0.5673	N3	-0.6323	-0.6545
C5'	0.0558	-0.0184	C4	0.1222	0.2101
H5'1	0.0679	0.0887	C3'	0.2022	0.2940
H5'2	0.0679	0.0887	O3'	-0.6541	-0.7637
C4'	0.1065	0.2567	H3T	0.4376	0.4748
H4'	0.1174	0.1060	H3'	0.0615	0.0751
O4'	-0.3548	-0.5344	C2'	0.0670	0.0900
C1'	0.0191	0.2909	H2'1	0.0972	0.1187
H1'	0.2006	0.0952	O2'	-0.6139	-0.7360
N9	0.0492	-0.1034	HO'2	0.4186	0.4670

Section S1: The script for using the new parameters.

1. Create a TOP file using the command "tleap -f tleap.in":

```
addatomtypes {"O3""O""sp2"}
addatomtypes {"O2""O""sp2"}
addatomtypes {"O""O""sp2"}
addatomtypes {"OW""O""sp3"}
addatomtypes {"OY""O""sp3"}
source leaprc.*                # Load protein force fields you want
source leaprc.water.tip3p      # Load water models
loadAmberPrep ATP-HF/B3.prepi  # Load prep file
loadAmberParams ATP-HF/B3.frcmod # Load frcmod file
.....                          # Other operations
saveamberparm name *.prmtop *.inpcrd
quit
```

2. Use "mod.py" to modify vdW parameters and add CMAP parameters:

Please install parmed and numpy extral python packages. The Python version needs to be greater than 3.6.

```
python mod.py -top *.prmtop -out *-out.prmtop -method B3LYP/HF
```